

Two regimes of dilute turbulent settling suspensions under shear

Jake Langham* and Andrew J. Hogg

School of Mathematics, Fry Building, University of Bristol, Bristol, BS8 1UG, UK

(Dated: October 13, 2023)

When turbulent flow is laden with negatively buoyant particles, their mean distribution over the direction of gravity can induce stable density gradients that penalize turbulent fluctuations. This effect is studied numerically for shear-driven flow with dilute non-inertial sediment. The turbulent dynamics and sediment transport depend critically on particle settling velocity v_s , splitting into two regimes: homogeneous weakly stratified turbulence and flow with developed turbulence atop an intermittent boundary layer. At intermediate v_s , neither state can be sustained and the flow laminarizes.

It is common for flows in nature to carry suspensions of fine particles over great distances. Examples abound in the atmosphere, rivers, coastlines and on the ocean floor [1–6]. Transport fluxes of suspended sediments have long been studied [7–9], due to their practical importance in engineering, as well as the substantial contribution they make to the Earth’s sediment cycle [10–13]. It is the turbulent fluctuations within a flow that are responsible for lifting particles into suspension and resisting their downward settling under gravity so that they can be transported. Less widely appreciated are the effects of suspensions on turbulence itself. Since work must be done by the flow against gravity in order to keep negatively buoyant sediment in suspension, even very dilute concentrations of settling particles are reported to reduce the intensity of turbulent fluctuations [14–18].

Efforts to probe this effect in detail using direct numerical simulations (DNS) of turbulence are far less common than for the related case of flows stratified by gradients in temperature or solute concentration, where the onset, development and characteristics of turbulence have been extensively studied for different canonical flow configurations (see e.g. [19–26]). For dilute sediment suspensions, research in this direction has predominantly focussed on channel flow models of gravity-driven turbidity currents [27–31]. Investigation of turbulence suppression reveals the essential mechanisms at play: clouds of settling particles preferentially concentrate towards lower depths and extract turbulent kinetic energy from the flow via the vertical fluxes required to maintain their average elevation. Sediments with settling velocities or densities exceeding a critical threshold laminarize the flow due to the coupled contributions of stable density stratification and localization of the flow driving force towards the bottom wall [28, 30]. Simulations of pressure driven [32, 33] and oscillatory channels [34], where this latter effect is not present, have hinted at similar bounds for partial or full laminarization, contingent on the suspension properties. In this Letter, we report the case of shear-driven flow. A new turbulent regime is identified that exists beyond the theoretical laminarization boundary and its properties are investigated.

We consider an incompressible fluid sheared between two infinite parallel planes perpendicular to gravity—a stationary basal surface and an upper wall moving with velocity $2U\mathbf{e}_x$. The flow is laden with negatively buoyant sediment particles, which settle under gravity with characteristic velocity $V_s\mathbf{e}_y$. We assume the sediment to be sufficiently small and dilute that

it occupies a continuous phase within the channel, for which the physics of particle inertia, cohesion and inter-particle collisions may be safely neglected. If density variations within the mixture are small, relative to the mean flow density, the Boussinesq approximation applies and the system obeys the following equations for the flow velocity $\mathbf{u}(\mathbf{x}, t)$, pressure $p(\mathbf{x}, t)$ and sediment concentration $c(\mathbf{x}, t)$, rendered dimensionless with respect to length and time scales H and H/U , where $2H$ is the channel height:

$$\frac{\partial \mathbf{u}}{\partial t} + \mathbf{u} \cdot \nabla \mathbf{u} = -\nabla p + Re^{-1} \nabla^2 \mathbf{u} - Ri_b c \mathbf{e}_y, \quad (1)$$

$$\nabla \cdot \mathbf{u} = 0, \quad (2)$$

$$\frac{\partial c}{\partial t} + \mathbf{u} \cdot \nabla c - v_s \frac{\partial c}{\partial y} = \kappa \nabla^2 c. \quad (3)$$

The dimensionless parameters are the bulk Reynolds number $Re = UH/\nu$, bulk Richardson number $Ri_b = M(\varrho - 1)gH/U^2$, dimensionless settling velocity $v_s = V_s/U$ and sediment diffusivity $\kappa = K/UH$, where ν is the viscosity of the fluid, g is gravitational acceleration, M is the mean volume fraction occupied by sediment, ϱ is the ratio of sediment and fluid densities and K is an effective dimensional sediment diffusivity which captures the aggregated effect of small, hydrodynamically mediated fluctuations of individual particle trajectories [30, 35, 36].

We perform DNS of Eqs. (1)–(3) within the computational domain $[0, L_x] \times [0, 2] \times [0, L_z]$, with $(L_x, L_z) = (4\pi, 2\pi)$. Periodic boundary conditions are enforced at $x = 0, L_x$ and $z = 0, L_z$. At the walls $y = 0, 2$, we fix no-slip conditions for the fluid, $\mathbf{u}(x, 0, z) = \mathbf{0}$ and $\mathbf{u}(x, 2, z) = 2\mathbf{e}_x$, and the no-flux condition $v_s c + \kappa \partial c / \partial y = 0$ for the sediment. For our simulations, we use the parallel pseudo-spectral ChannelFlow code [37], adapted to integrate Eqs. (1)–(3) with 330×256 de-aliased Fourier modes in (x, z) and 141 Chebyshev modes in y . We fix $Re = 3125$ and $\kappa = 3.2 \times 10^{-4}$ throughout, which implies unit Schmidt number $Sc = (Re\kappa)^{-1}$.

Throughout this Letter, quantities averaged over the horizontal coordinates x & z are adorned with an overbar $\bar{\cdot}$, with primes denoting fluctuations away from this mean, e.g. velocity fluctuations are $\mathbf{u}' = \mathbf{u} - \bar{\mathbf{u}}$ and the total instantaneous turbulent kinetic energy (TKE) for the flow is $\frac{1}{4} \int_0^2 \overline{\mathbf{u}' \cdot \mathbf{u}'} dy$. Angular brackets $\langle \cdot \rangle$ denote time averages, which are taken over at least 2000 advective time units when reporting DNS data.

To demonstrate the effect of the settling particle field on turbulence, we begin with an illustrative numerical experi-

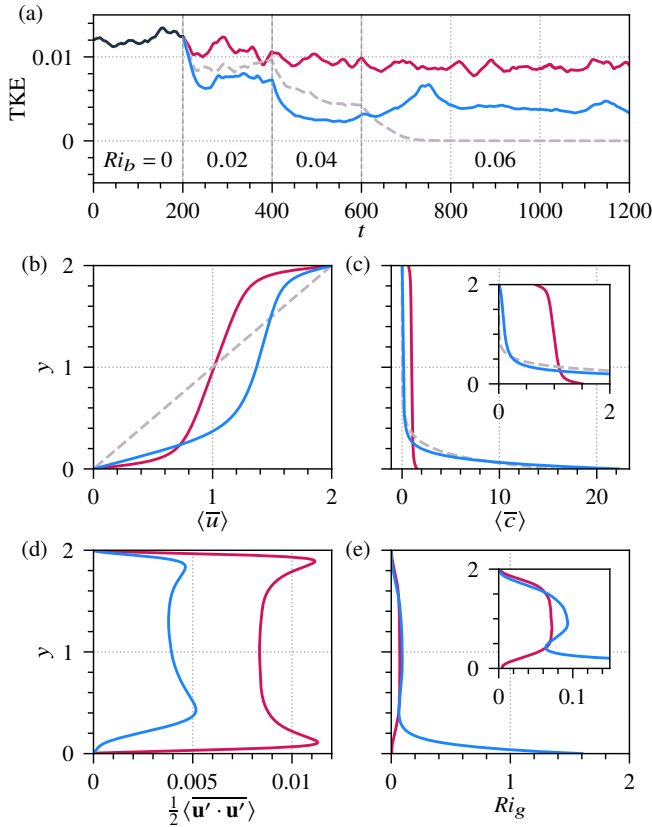


FIG. 1: Development of turbulence into distinct regimes, depending on settling velocity, $v_s = 10^{-3}$ (solid red), 2.5×10^{-3} (dashed gray) and 4×10^{-3} (solid blue). (a) Total TKE evolution for an initially unstratified flow (solid black, $0 \leq t < 200$), incrementally subjected to increasing $Ri_b = 0.02$ ($200 \leq t < 400$), 0.04 ($400 \leq t < 600$) and 0.06 ($t \geq 600$). Panels (b)–(e) show the wall-normal dependence of selected mean quantities, upon reaching steady state, at $Ri_b = 0.06$: (b) streamwise velocity, (c) concentration, (d) TKE and (e) gradient Richardson number, Ri_g .

ment. From a state of fully developed unstratified turbulence, containing neutrally buoyant sediment with settling velocities $v_s = 10^{-3}$, 2.5×10^{-3} and 4×10^{-3} , we increase Ri_b from zero to 0.06, in increments of 0.02 separated by 200 advective time units. In Fig. 1(a), the resultant TKE for the three flows is plotted. The flows with lowest and highest v_s reach statistically steady states, following losses of TKE after the introduction of buoyancy effects. In contrast, the middle state cannot maintain turbulence and laminarizes. The ultimate steady-state streamwise velocity $\langle \bar{u} \rangle$ and concentration $\langle \bar{c} \rangle$ profiles are plotted in Figs. 1(b) and 1(c) respectively. Moreover, in Figs. 1(d) and (e), we respectively show the y -dependence of both the mean turbulent kinetic energy and gradient Richardson number $Ri_g = -Ri_b (d\langle \bar{c} \rangle / dy) / (d\langle \bar{u} \rangle / dy)^2$. In the simulation with lowest v_s (10^{-3}), the profiles exhibit approximate symmetry about the centerline. Settling induces higher concentrations towards the bottom wall, leading to an emergent bulk stratification, which is reorganized by turbulence, ultimately leaving profiles that resemble simulations of stably stratified shear

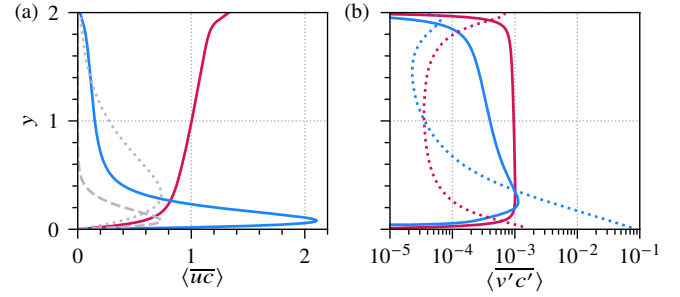


FIG. 2: Concentration correlations for a WS flow with $v_s = 10^{-3}$ (red) and SBL flow with $v_s = 4 \times 10^{-3}$ (blue). In both cases, $Ri_b = 0.06$. (a) Streamwise sediment transport. The gray lines display the equivalent values for laminar flow with $v_s = 10^{-3}$ (dotted) and $v_s = 4 \times 10^{-3}$ (dashed). (b) Vertical turbulent sediment flux (solid lines). Also shown is $-\kappa d\langle \bar{c} \rangle / dy$ (dotted lines).

flows [23, 24]. Conversely, in the case of highest settling velocity (4×10^{-3}), most of the sediment is contained within a narrow boundary layer ($0 \leq y \leq 0.4$). Turbulent activity is suppressed over this region [see Fig. 1(d)], as may be expected from the high concentration gradients at the bottom wall. Nevertheless, turbulence persists in the relatively dilute upper channel, which feels a similar, but slightly stronger level of stratification than the low v_s case. In the intermediate case, v_s (2.5×10^{-3}) is neither low enough that the flow becomes only weakly stratified, nor high enough to drive sufficient quantities of sediment out of the upper channel and turbulence is fully extinguished.

The turbulent flows described above are archetypes of two broad regimes we identify from our simulations. The first regime, which governs flows when v_s or Ri_b are sufficiently small (but positive), we refer to as ‘weakly self-stratified’ (WS) and shares some characteristics with pressure and gravity-driven simulations conducted by Cantero and co-workers using the same governing equations [27, 32]. The second regime, which exists beyond the laminarization boundary for WS flows, is yet to be identified in prior studies. We refer to these flows, in which turbulence sustains itself above a strongly-stratified near-bed region, as sediment boundary layer (SBL) turbulence.

Of particular interest in applications is the rate of sediment transported along the channel. In Fig. 2(a), we plot the streamwise sediment flux for our example WS and SBL flows. The flux for the WS flow monotonically increases with y , attaining its maximum at the top of the channel. In contrast, the SBL flow transports most of its sediment within the boundary layer at the bottom wall. Though the no-slip boundary causes u to be relatively low in this region, high near-wall concentration leads to a peak streamwise flux at $y \approx 0.08$. In both cases, we find that the contribution from the turbulent streamwise flux $\langle u'c' \rangle$ (not plotted) is negligible ($|\langle u'c' \rangle| < 0.025 \langle \bar{u} \bar{c} \rangle$). Nevertheless, turbulent fluctuations are important due to the role they play in adjusting the mean flow and concentration profiles away from laminar flow. On averaging the x -directed component of Eqs. (1) and (3) over x , z and t , one obtains (after integrating

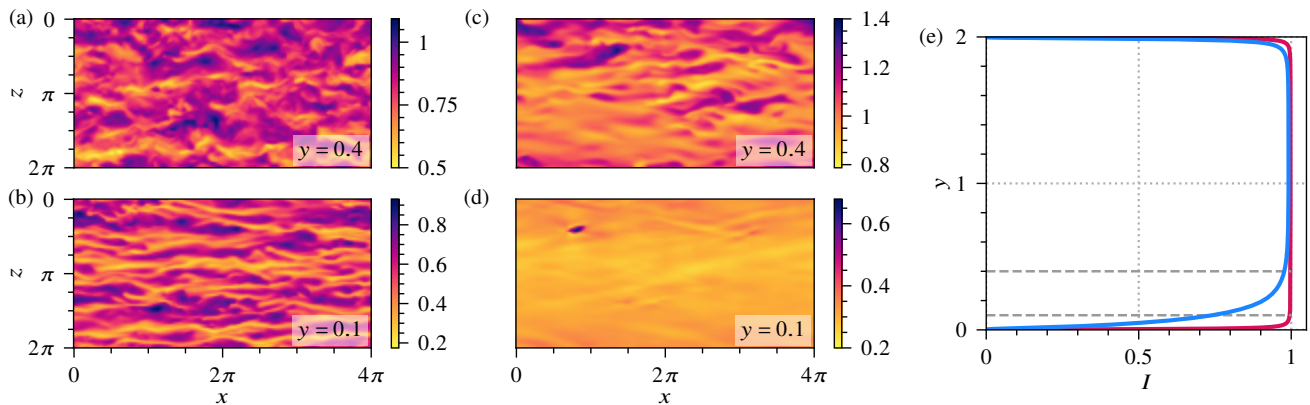


FIG. 3: Intermittency near the bottom wall. (a)–(d) Horizontal slices for the WS (a,b) and SBL (c,d) example flows, at $y = 0.4$ (a,c) and $y = 0.1$ (b,d), showing the instantaneous streamwise velocity field u as a function of x and z . Snapshots (a,b) and (c,d) are taken at the same time instant. (e) Dependence of intermittency factor I on y for the example WS (red) and SBL (blue) flows. Dashed gray lines are at $y = 0.1, 0.4$.

in y)

$$\frac{d\langle \bar{u} \rangle}{dy} - \frac{d\langle \bar{u} \rangle}{dy} \Big|_{y=0} = Re\langle \bar{u}'v' \rangle, \quad (4)$$

$$\kappa \frac{d\langle \bar{c} \rangle}{dy} + v_s \langle \bar{c} \rangle = \langle \bar{v}'c' \rangle, \quad (5)$$

with $\langle \bar{u} \rangle = u = y$ and $\langle \bar{c} \rangle = c = \frac{v_s}{\kappa} \exp[v_s(1-y)/\kappa] / \sinh(v_s/\kappa)$, when flow is laminar. The streamwise sediment fluxes for these solutions are included in Fig. 2(a) in gray, for the two v_s values corresponding to the example WS and SBL flows. In each case, the flux is everywhere enhanced by turbulence. In the WS flow, this is primarily due to turbulent vertical concentration fluxes making more sediment available in the upper channel, $y \gtrsim 0.4$. In the SBL flow, this effect is important too—streamwise flux in the region $y > 0.4$ accounts for roughly one third of $\frac{1}{2} \int_0^2 \langle \bar{u}\bar{c} \rangle dy$. Furthermore, via Eq. (4), turbulent modification of the mean flow [plotted in Fig. 1(b)] by the Reynolds stress $\langle \bar{u}'v' \rangle$ (not shown) enhances transport within the boundary layer. To complement this picture, in Fig. 2(b), we plot $\langle \bar{v}'c' \rangle$ and $-\kappa d\langle \bar{c} \rangle / dy$. We see that the WS concentration profile is primarily dictated by near constant uplift from vertical turbulent fluxes [balancing the settling term $v_s \langle \bar{c} \rangle$ in Eq. (5)] except very close to the walls, where sediment diffusion takes over. In the SBL case, there is a clear separation between the diffusively dominated boundary layer, where the peak streamwise flux occurs, and the turbulent suspension in the upper channel.

While turbulence is greatly suppressed within the sediment boundary layer, it may intrude from the upper channel, where TKE is higher. Both the mixing of streamwise momentum and the mixing of concentration between these two regions occur in a spatiotemporally intermittent way. This may be visualized by viewing channel slices at different depths. In Figs. 3(a)–(d), we plot horizontal cross-sections of the u field for the example WS (a,b) and SBL (c,d) flows at $y = 0.4$ and $y = 0.1$. The WS flow is well developed at $y = 0.4$, with streaky near-wall structures at $y = 0.1$ that qualitatively resemble their well-studied

counterparts in unstratified shear flows [38–40]. In contrast, the SBL turbulence is patchy at $y = 0.4$ (the edge of the sediment boundary layer). At $y = 0.1$, the flow is essentially quiescent, except for an isolated spot of faster fluid advected into the boundary layer from above. The plotted snapshots are broadly representative of the sustained flow dynamics, which feature a tension between the transient proliferation of turbulent structures and their suppression by high concentration gradients. To measure this phenomenon, we compute the average turbulent fraction at each height, by computing the intermittency factor $I(y) = \langle \chi(\mathbf{u}) \rangle$, where χ is an indicator function defined to be 1 if the TKE exceeds 10^{-4} and zero otherwise. (Other choices for χ lead to qualitatively similar conclusions.) We plot $I(y)$ in Fig. 3(e). For both flows, $I(y) \approx 1$ throughout the channel interior, falling to $I(y) = 0$ at the walls. The length scale over which this occurs is dictated by the thickness of the viscous boundary layers for each fluid, except in the case of SBL flow at the bottom wall, for which $I(y)$ transitions comparatively slowly from 0 to 1 over $0 \leq y \leq 0.4$.

Since the SBL flow is intermittent in the region containing most of the sediment, this has implications for the transport. In Figs. 4(a,b), we compare two illustrative snapshots of $v'c' / \langle \bar{v}'c' \rangle$ for (a) WS and (b) SBL flow. The WS fluxes are comprised of many upward and downward contributions, which exhibit some streamwise alignment and are distributed homogeneously throughout the channel. In contrast, the SBL fluxes consist of a few comparatively large events scattered within the regions where turbulent intensity is high [see Fig. 3(c)]. In Fig. 4(c), the corresponding probability density function (p.d.f) is plotted for both flows. The probability mass of both distributions is highly concentrated around zero, with rapidly decaying tails that count rarer, but more significant fluxes. As expected, the tails for SBL flow are wider and greater magnitude. In both cases, $\langle \bar{v}'c' \rangle$ is a sum of nearly canceling positive and negative contributions that are slightly positively skewed to produce an upward net flux that balances settling and diffusion [Eq. (5)]. To identify which events tip the balance, we plot in Fig 4(d) the difference between the positive

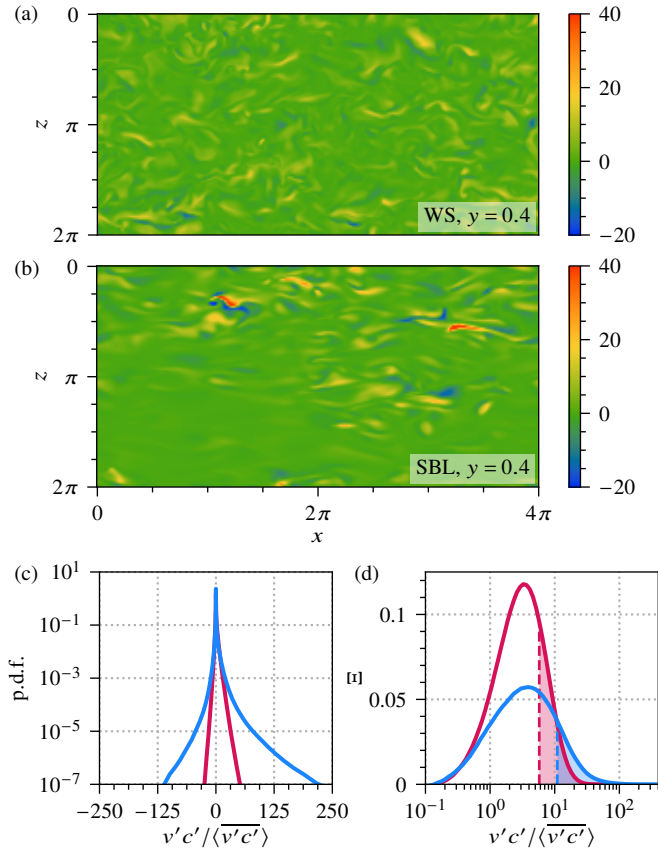


FIG. 4: Intermittency of vertical sediment transport. (a,b) Example horizontal cross-sections of $v'c'/\langle v'c' \rangle$ at $y = 0.4$ for (a) WS and (b) SBL flows, taken at the same time instant as the snapshots in Fig. 3. The color scale is thresholded between -20 and 40 to improve visual clarity across the two panels. This clips both ends of the SBL slice, which attains a minimum of -40.8 and a maximum of 86.7 (3 s.f.). Panels (c) and (d) plot statistics for the WS (solid red) and SBL (solid blue) cases: (c) p.d.f. of $\mu = v'c'/\langle v'c' \rangle$; (d) $\Xi(\mu) = \mu[f(\mu) - f(-\mu)]$, where f is the p.d.f. of μ . The shaded regions divide the area under each curve in half.

and negative halves of the p.d.f., weighted by the corresponding (normalized) magnitude of vertical flux. This quantifies the net contribution due to upward fluxes of a given size, to the mean of $v'c'$, after subtracting off parts that cancel with equal and opposite downward fluxes. Both datasets are divided into two groups, which contribute equally to the mean. Despite their importance to maintaining the suspension, the higher flux events comprise less than 6% and 3% of the probability masses of the WS and SBL p.d.f.s respectively.

The observations made thus far qualitatively generalize as Ri_b and v_s are varied away from our chosen example values. To demonstrate this, we have conducted extensive numerical investigations of parameter space. The data are summarized in Fig. 5. Points on these axes are plotted with circles if DNS remained in a statistically steady state with nonzero TKE for at least 1000 advective time units. Each simulation was initiated from a developed turbulent state at nearby parameter values (starting from passive scalar flows at $Ri_b = 0$). Guided by

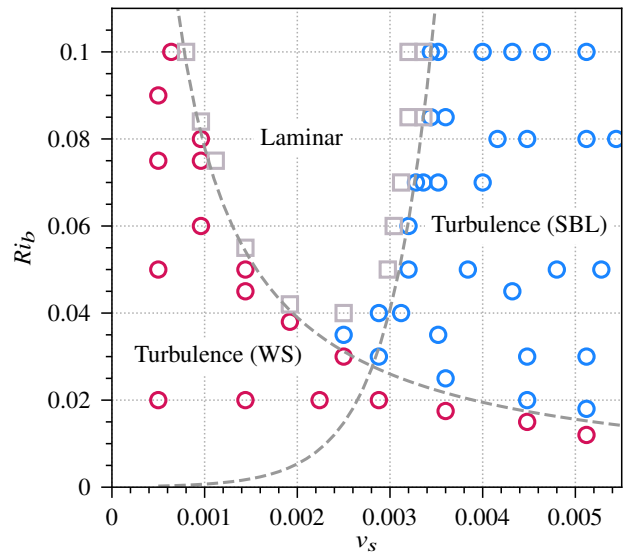


FIG. 5: Laminar-turbulent boundary. Circles plot (v_s, Ri_b) pairs, for which DNS maintains statistically steady WS (red) or SBL (blue) turbulence. Squares show parameters for which we were unable to find a sustained turbulent flow. The dashed gray lines separating the regimes are the curves $Ri_b = A/v_s$ and $Ri_b = B \exp(v_s y^*/\kappa)$, with $A = 7.8 \times 10^{-5}$, $B = 9.2 \times 10^{-5}$ and $y^* = 0.65$.

Fig. 1(e), we classify flows as SBL turbulence if $\max_y Ri_g$ occurs at the lower wall and WS otherwise. Within each regime, we find flow statistics that are qualitatively similar to those of the example flows reported in Figs. 1 and 2.

Runs that decayed to laminar flow are plotted with squares on Fig. 5. Tracing the laminar-turbulent boundary requires care, because the process of decay to the laminar state is stochastic. Moreover, for initial conditions far from the turbulent attractor it can be the case that turbulence is fully suppressed before the concentration field has time to statistically equilibrate to a state that would otherwise permit turbulence. For these reasons, each point straddling the boundary was initiated by varying Ri_b by no more than 5×10^{-3} , or v_s by no more than 2×10^{-4} , from an established turbulent flow and integrating for at least 2000 time units. In the intermittent SBL regime, runs of up to 10000 units were employed.

Two fitted curves (dashed gray) plotted on Fig. 5 separate the regimes. In the WS case, analysis of the TKE budget suggests that turbulence cannot be sustained globally if $Ri_b v_s$ exceeds a threshold value [28]. Beyond this, the flow must either fully laminarize, or enough sediment must drop out of suspension for the turbulence to survive above the boundary layer, as happens for $v_s \gtrsim 2.5 \times 10^{-3}$. In the SBL regime, the upper channel becomes increasingly diluted at higher settling velocities and the laminar-turbulent boundary rises acutely, following an empirically determined exponential dependence.

At higher Re , it may be anticipated that the laminar region retreats towards higher Ri_b , just as the corresponding laminarization threshold does in thermally stratified shear flow [23]. However, we hypothesize that the WS and SBL flow regimes

qualitatively persist, since the mechanisms that separate them are not specific to moderate- Re turbulence. Though the dilute continuum model considered herein does not attempt to describe the full physics of fluid-sediment interactions, our results capture some essential features of environmental flows. For example, flows in river channels have been observed to bifurcate into transport regimes that carry sediment in suspension and in a localized near-bed layer [41]. In this setting, the commonly applied diffusive term in Eq. (3) could be viewed as a phenomenological closure, which promotes a basal ‘reservoir’ of sediment that can be ejected into suspension by turbulent fluctuations. The striking spatiotemporal intermittency of this process, as demonstrated in Fig. 4, suggests a need to move beyond descriptions of sediment transport that average over transient flow structures.

The authors acknowledge funding from EPSRC New Horizons grant EP/V049054/1. We are grateful to Robert M. Dorell and Charlie J. Lloyd for useful discussions and initially prompting us to investigate self-stratifying flows. This work was carried out using the computational facilities of the Advanced Computing Research Centre, University of Bristol.

* j.langham@bristol.ac.uk

- [1] K. Schepanski, *Geosciences* **8**, 151 (2018).
- [2] O. Korup, *Earth-Sci. Rev.* **112**, 115 (2012).
- [3] L. A. Martinelli, R. L. Victoria, A. H. Devol, J. E. Richey, and B. R. Forsberg, *GeoJournal* **19**, 381 (1989).
- [4] L. C. Van Rijn, J. S. Ribberink, J. V. D. Werf, and D. J. R. Walstra, *J. Hydraul. Res.* **51**, 475 (2013).
- [5] T. Mulder, J. P. M. Syvitski, S. Migeon, J.-C. Faugères, and B. Savoye, *Mar. Petrol. Geol.* **20**, 861 (2003).
- [6] E. Meiburg and B. Kneller, *Ann. Rev. Fluid Mech.* **42**, 135 (2010).
- [7] L. C. van Rijn, *J. Hydraul. Eng.* **110**, 1613 (1984).
- [8] K. R. Dyer and R. L. Soulsby, *Ann. Rev. Fluid Mech.* **20**, 295 (1988).
- [9] R. Soulsby, *Dynamics of marine sands* (T. Telford London, UK, 1997).
- [10] B. Elfrink and T. Baldock, *Coast. Eng.* **45**, 149 (2002).
- [11] S. R. Gislason, E. H. Oelkers, and Á. Snorrason, *Geology* **34**, 49 (2006).
- [12] E. N. Dethier, C. E. Renshaw, and F. J. Magilligan, *Science* **376**, 1447 (2022).
- [13] J. Syvitski, J. R. Ángel, Y. Saito, I. Overeem, C. J. Vörösmarty, H. Wang, and D. Olago, *Nat. Rev. Earth Env.* **3**, 179 (2022).
- [14] C. Villaret and J. H. Trowbridge, *J. Geophys. Res.: Oceans* **96**, 10659 (1991).
- [15] J. C. Winterwerp, *J. Geophys. Res.: Oceans* **106**, 22559 (2001).
- [16] J. Tu, D. Fan, Y. Zhang, and G. Voulgaris, *J. Geophys. Res.: Oceans* **124**, 4058 (2019).
- [17] G. Egan, A. J. Manning, G. Chang, O. Fringer, and S. Monismith, *J. Geophys. Res.: Oceans* **125**, e2019JC016022 (2020).
- [18] R. Huang, Q. Zhang, W. Zhang, and Z. Li, *Estuar., Coast. Shelf Sci.* **278**, 108128 (2022).
- [19] C. P. Caulfield and W. R. Peltier, *J. Fluid Mech.* **413**, 1 (2000).
- [20] W. D. Smyth and J. N. Moum, *Phys. Fluids* **12**, 1343 (2000).
- [21] M. Garcia-Villalba and J. C. Del Alamo, *Phys. Fluids* **23** (2011).
- [22] G. Brethouwer, Y. Duguet, and P. Schlatter, *J. Fluid Mech.* **704**, 137 (2012).
- [23] E. Deusebio, C. P. Caulfield, and J. R. Taylor, *J. Fluid Mech.* **781**, 298 (2015).
- [24] Q. Zhou, J. R. Taylor, and C. P. Caulfield, *J. Fluid Mech.* **820**, 86 (2017).
- [25] D. Lucas, C. P. Caulfield, and R. R. Kerswell, *J. Fluid Mech.* **868**, 97 (2019).
- [26] A. K. Kaminski and W. D. Smyth, *J. Fluid Mech.* **862**, 639 (2019).
- [27] M. I. Cantero, S. Balachandar, A. Cantelli, C. Pirmez, and G. Parker, *J. Geophys. Res.: Oceans* **114** (2009).
- [28] M. I. Cantero, M. Shringarpure, and S. Balachandar, *Geophys. Res. Lett.* **39** (2012).
- [29] M. I. Cantero, A. Cantelli, C. Pirmez, S. Balachandar, D. Mohrig, T. A. Hickson, T. Yeh, H. Naruse, and G. Parker, *Nat. Geosci.* **5**, 42 (2012).
- [30] M. Shringarpure, M. I. Cantero, and S. Balachandar, *J. Fluid Mech.* **712**, 384 (2012).
- [31] C. E. Ozdemir and X. Yu, *Phys. Fluids* **30** (2018).
- [32] M. I. Cantero, S. Balachandar, and G. Parker, *J. Turbul. p. N27* (2009).
- [33] S. Dutta, M. I. Cantero, and M. H. García, *Earth Surf. Dynam.* **2**, 419 (2014).
- [34] C. E. Ozdemir, T.-J. Hsu, and S. Balachandar, *J. Fluid Mech.* **665**, 1 (2010).
- [35] F. Necker, C. Härtel, L. Kleiser, and E. Meiburg, *Int. J. Multiphas. Flow* **28**, 279 (2002).
- [36] É. Guazzelli and J. Hinch, *Ann. Rev. Fluid Mech.* **43**, 97 (2011).
- [37] J. F. Gibson, F. Reetz, S. Azimi, A. Ferraro, T. Kreilos, H. Schrobbsdorff, M. Farano, A. F. Yesil, S. S. Schütz, M. Culp, et al. (2023), in preparation, see <https://www.channelflow.ch>.
- [38] P. Moin and J. Kim, *J. Fluid Mech.* **118**, 341 (1982).
- [39] S. K. Robinson, *Ann. Rev. Fluid Mech.* **23**, 601 (1991).
- [40] J. Jiménez, J. C. Del Alamo, and O. Flores, *J. Fluid Mech.* **505**, 179 (2004).
- [41] H. Ma, J. A. Nittrouer, B. Wu, M. P. Lamb, Y. Zhang, D. Mohrig, X. Fu, K. Naito, Y. Wang, A. J. Moodie, et al., *PNAS* **117**, 171 (2020).